

A Moist Static Energy Budget Analysis of Quasi-2-Day Waves Using Satellite and Reanalysis Data

YUKARI SUMI

Graduate School of Environmental Studies, Nagoya University, Nagoya, Japan

HIROHIKO MASUNAGA

Hydrospheric Atmospheric Research Center, Nagoya University, Nagoya, Japan

(Manuscript received 29 March 2015, in final form 23 October 2015)

ABSTRACT

A moist static energy (MSE) budget analysis is applied to quasi-2-day waves to examine the effects of thermodynamic processes on the wave propagation mechanism. The 2-day waves are defined as westward inertia–gravity (WIG) modes identified with filtered geostationary infrared measurements, and the thermodynamic parameters and MSE budget variables computed from reanalysis data are composited with respect to the WIG peaks. The composite horizontal and vertical MSE structures are overall as theoretically expected from WIG wave dynamics. A prominent horizontal MSE advection is found to exist, although the wave dynamics is mainly regulated by vertical advection. The vertical advection decreases MSE around the times of the convective peak, plausibly resulting from the first baroclinic mode associated with deep convection. Normalized gross moist stability (NGMS) is used to examine the thermodynamic processes involving the large-scale dynamics and convective heating. NGMS gradually decreases to zero before deep convection and reaches a maximum after the convection peak, where low (high) NGMS leads (lags) deep convection. The decrease in NGMS toward zero before the occurrence of active convection suggests an increasingly efficient conversion from convective heating to large-scale dynamics as the wave comes in, while the increase afterward signifies that this linkage swiftly dies out after the peak.

1. Introduction

Quasi-2-day waves are tropical atmospheric disturbances with a period of about 2 days. Their dynamics are explained by a convectively coupled $n = 1$ westward inertia–gravity wave (WIG1) (Matsuno 1966; Takayabu 1994a). A quasi-2-day wave typically has a phase speed of about $10\text{--}30\text{ m s}^{-1}$, a zonal wavelength of about 2000–4000 km, and an equivalent depth of about 12–50 m (Takayabu 1994b; Takayabu et al. 1996; Chen et al. 1996; Haertel and Johnson 1998; Wheeler and Kiladis 1999; Wheeler et al. 2000; Kiladis et al. 2009; Haertel and Kiladis 2004; Haertel et al. 2008). A 2-day wave has distinct developing stages associated with progress in the representative cloud types from shallow cumuli to deep convective and stratiform clouds

(Takayabu et al. 1996; Chen and Houze 1997; Mapes et al. 2006). These stages are common to convectively coupled equatorial waves (CCEWs), Madden–Julian oscillation (MJO), and mesoscale convective systems (Houze 2004; Kikuchi and Takayabu 2004; Mapes et al. 2006).

In past 15 yr, theoretical models of CCEWs have been developed with a focus on multiple vertical modes having different heating profiles. Mapes (2000) proposed a “stratiform instability” mechanism where a lower-tropospheric cooling by the second baroclinic mode could give rise to an unstable growth working together with upper-tropospheric heating and lower-tropospheric cooling in stratiform precipitation. Haertel and Kiladis (2004) and Haertel et al. (2008) examined the variations of environmental fields in 2-day waves and MJO by using the two-mode model whose basic states are given by Tropical Ocean and Global Atmosphere Coupled Ocean–Atmosphere Response Experiment (TOGA COARE) intensive operative period (IOP) data. Kuang (2008) discussed the “moisture

Corresponding author address: Yukari Sumi, Graduate School of Environmental Studies, Nagoya University, Furo-cho Chikusa-ku, Nagoya 464-8601, Japan.
E-mail: sumi@satellite.hyarc.nagoya-u.ac.jp

stratiform instability” mechanism that relies on a moisture increase in the middle troposphere preceding deep convection as a driver of CCEWs.

In fact, observational investigations have indicated that a moisture increase in the middle troposphere plays a key role in the development of deep convection accompanied with CCEWs and MJO (Kiladis et al. 2009; Benedict and Randall 2007). Tropical deep convection and tropospheric moisture are known to be closely linked to each other from a variety of observational studies (Sherwood 1999; Bretherton et al. 2004; Peters and Neelin 2006; Holloway and Neelin 2009). In line with these observational implications, the relationship between tropospheric moisture and convective development has been built in some recent theoretical models (Neelin and Yu 1994; Raymond 2000; Sobel et al. 2001; Fuchs and Raymond 2007; Kuang 2008). Equatorial wave modes theorized along this line are often called a “moisture mode.” A series of recent studies discussed the MJO dynamics in terms of moisture modes (Maloney 2009; Kiranmayi and Maloney 2011; Andersen and Kuang 2012; Benedict et al. 2014; Kim et al. 2014; Sobel et al. 2014; Maloney et al. 2010). Meanwhile, quasi-2-day waves have drawn far less attention than MJO with a few exceptions (Haertel and Kiladis 2004; Haertel et al. 2008) and have yet to be studied particularly in light of the potential importance of tropospheric moisture. In this study, the thermodynamic processes in quasi-2-day waves are analyzed for clarifying their relevance to the wave propagation mechanism. To this end, a moist static energy (MSE) budget analysis is applied to quasi-2-day waves.

This paper consists of the following sections. In section 2, the data and composite methods are described. In section 3, features of spatiotemporal variations of convection and environmental fields are shown in detail. In section 4, the thermodynamic in quasi-2-day waves are examined from MSE budget analysis. In section 5, discussion and summary are presented.

2. Data and methods

a. Data

Global-merged IR brightness temperature (TBB) data (mergedIR) is used for identifying quasi-2-day waves. The mergedIR is gridded global data in which *Geostationary Operational Environmental Satellite (GOES)-9/10*, *Meteorological Satellite (Meteosat)-7/1-5*, and *Geostationary Meteorological Satellite (GMS)* are combined (Janowiak et al. 2001). The temporal resolution is 30 min and the horizontal resolution is 0.0364° .

The surface precipitation data is obtained from Tropical Rainfall Measuring Mission (TRMM) data

product. TRMM satellite is a sun-asynchronous satellite orbiting with an inclination angle of about 35° and carrying the Precipitation Rader (PR). The horizontal and vertical resolutions of PR are about 4 km and 250 m, respectively. The near-surface precipitation data in PR2A25 level 2, version 6, is used (Iguchi et al. 2000). Convective and stratiform precipitation types are separated.

ERA-Interim (ERA-I) data is one of European Centre for Medium-Range Weather Forecasts (ECMWF)’s reanalysis datasets (Simmons et al. 2007). The horizontal resolution is 1.5° and the total number of pressure levels is 38. The temporal resolution is 6 and 12 h for three- and two-dimensional data, respectively. To calculate MSE budget terms, various ERA-I data are utilized in this study (see section 4): 1) the three-dimensional variables: geopotential height ϕ , temperature T , specific humidity q , horizontal wind velocity vector $\mathbf{V} = (u, v)$, and pressure velocity ω and 2) the two-dimensional variables: surface sensible heat flux (SH), surface latent heat flux (LH), surface short-wave flux SW_s , short-wave flux at the top of the atmosphere (TOA) SW_t , surface long-wave flux LW_s , long-wave flux at TOA LW_t , and sea–land flag. Note that conclusions in this study hardly depend on the choice of reanalysis datasets (not shown). National Centers for Environmental Prediction (NCEP) Reanalysis-1 (Kalnay et al. 1996) and Japanese 25-year Reanalysis (JRA25) data (Onogi et al. 2007) have been tested and found to show no qualitative difference from ERA-I data.

In all datasets, the analysis period is the 10 yr between 2000 and 2009. The analysis area is the whole tropical region between 10°N and 10°S over oceans as selected with the sea–land flag. Also, all satellite data are projected onto a 0.25° grid.

b. Spectrum

Space–time spectrum analysis is performed on the high-resolution TBB data (mergedIR) produced from geostationary Earth-orbiting (GEO) satellites. TBB spectrum is calculated in a manner similar to that used by Wheeler and Kiladis (1999). First, raw TBB data are averaged over the latitudinal band between 10°N and 10°S . A longitude–time cross section of the area-averaged TBB is constructed for every 2 yr between 2000 and 2009. Missing data are filled in by linear interpolation over time. Second, anomalous values are obtained by removing the mean and the linear components at each longitude. Third, the time series of the anomaly are divided into 80-day segments that consecutively overlap each other by 40 days. Then, a split cosine bell tapering function is applied to each segment to avoid spectral leakage. Finally, fast Fourier transform

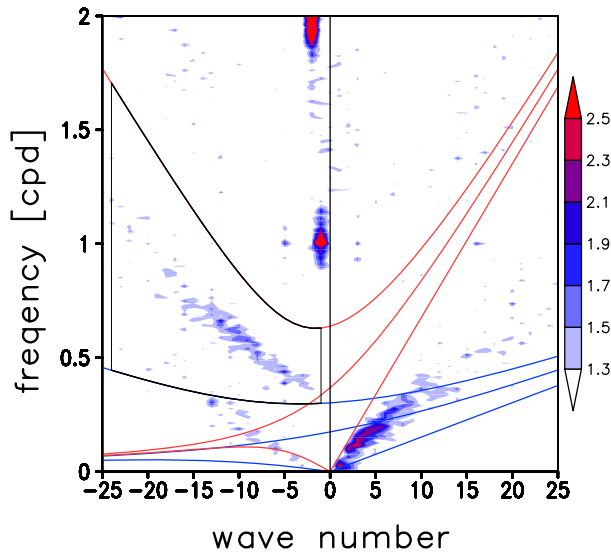


FIG. 1. The raw power spectrum normalized by the background spectrum (shaded) in wavenumber–frequency (cpd) domain. A negative (positive) wavenumber means westward (eastward) mode. Shading begins at a value of 1.3, which is significant at the 95% level with 91 DOF. The colored lines represent the dispersion relationships of various equatorial waves for different equivalent depths of 5 (blue) and 100 m (red): inertia–gravity wave ($n = 1$), Rossby wave ($n = 1$), mixed Rossby wave ($n = 0$), and Kelvin wave ($n = -1$). The large black frame represents the WIG filter used in this study, including $k = 1$ –24 and $h_e = 5$ –100 m.

(FFT) is performed to obtain the power spectrum of anomalous TBB for each segment. The power spectrum, with a frequency resolution f of 0.0125 (1/80) cycles per day (cpd) are averaged over 10 yr from 2000 to 2009.

Figure 1 shows the raw power spectrum normalized by the background spectrum in wavenumber–frequency domain. The background spectrum is computed by smoothing many times the raw spectrum with a 1–2–1 filter in frequency only. Here, the degree of freedom (DOF) is estimated about 91 ($\approx 2 \times 365 \times 10/80$). Shading begins at a value of 1.3, which is significant at the 95% level, based on a chi-squared test with 91 DOF. The normalized spectrum in Fig. 1 corresponds well to the equatorial wave signals in the previous studies (Wheeler and Kiladis 1999; Roundy and Frank 2004; Masunaga et al. 2006; Masunaga 2007; Kiladis et al. 2009; Tulich and Kiladis 2012; Yasunaga and Mapes 2012a,b). The westward-propagation domain includes the signals of WIG wave, equatorial Rossby wave, and tropical depression (TD)-type disturbances. Also, diurnal and semidiurnal disturbances are prominent. The eastward-propagation domain includes the signals of MJO and Kelvin wave.

c. Filtering

To isolate individual CCEW modes, Wheeler and Kiladis (1999) presented a wavenumber–frequency

filtering technique. They calculated power spectra from outgoing longwave radiation (OLR) data and defined the filters based on the dispersion curves of equatorial waves derived by Matsuno (1966). The similar technique has been widely used in previous studies based on OLR data, infrared brightness temperature data, precipitation data, and precipitable water data (Wheeler et al. 2000; Roundy and Frank 2004; Masunaga et al. 2006; Masunaga 2007; Kiladis et al. 2009; Yasunaga and Mapes 2012a,b).

This approach is applied to the present study with some minor modifications as described below. It is assumed that convectively coupled WIG wave is a practical indicator of a quasi-2-day wave. WIG signals are identified from space–time filtering analysis of TBB data. To isolate WIG waves, the $n = 1$ WIG filter is defined between $k = 1$ and 24 and two dispersion relationships with the equivalent depth h_e of 5 and 100 m (large black frame in Fig. 1). This filter is somewhat broader than WIG filters used in previous studies, although not including highest frequencies as examined by some recent works (Tulich and Kiladis 2012; Kikuchi 2014). The filter includes the strong WIG signals ($k \sim 10$, $f \sim 0.5$ –1) and stays outside the TD signals (e.g., Kiladis et al. 2006) that appear below the lower end of the filter near $f = 0.2$ –0.4 cpd. Therefore, TD-type disturbances are unlikely to severely affect in this analysis. To verify the justification for the WIG filter, we tested the same filter as defined in Wheeler and Kiladis (1999), including $k = 1$ –14 and $h_e = 17$ –50 m. The difference of the filter design does not change our results seriously (not shown).

Figure 2 is the longitude–time cross section during the period between December 2004 and January 2005 for an example to show how the filtering works. Unfiltered TBB (Fig. 2a) shows that a synoptic-scale envelope of active convection is prominent between the Indian Ocean (IO) and western Pacific Ocean (WP), while 2-day disturbances are only barely discernible. Westward-propagating 2-day waves are clearly captured in the WIG-filtered TBB (Fig. 2b), particularly striking in the western Pacific between 140°E and 180°.

d. Definition of the peak of WIG wave

A convective center of WIG wave is detected by utilizing a longitude–time cross section of filtered TBB data. First, zonal local minima of filtered TBB are searched at each time. Only a minimum locating at the center of a search area of $\pm 10^\circ$ is picked up, ignoring noisy fluctuations. All local minima are searched by moving the search area in zonal direction. Next, the minima colder than minus two standard deviations σ are defined as the longitudinal location of convective centers of WIG waves (WIG peaks). This threshold is used to prevent the composite WIG wave structures from

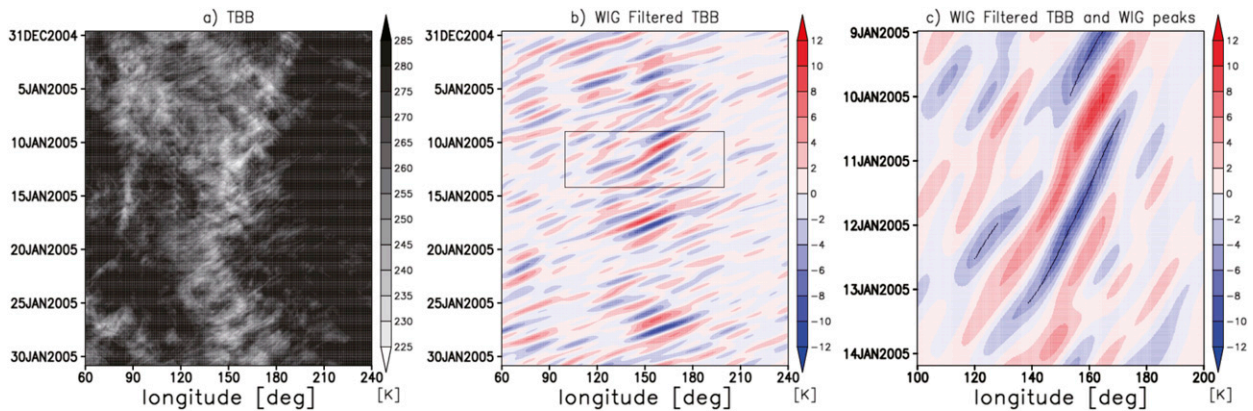


FIG. 2. A longitude–time cross section of (a) raw TBB, (b) WIG-filtered TBB, and (c) WIG-filtered TBB and WIG peaks (black dot). The area surrounded by a black box in (b) is displayed in a larger size in (c). The longitudinal band is between 60°E and 120°W. The time period is between 31 Dec 2004 and 31 Jan 2005.

being contaminated by irrelevant background convective signals. The standard deviation is computed from longitude–time cross section with the sample number of about 50 457 600 ($\sim 2 \times 365 \times 48 \times 360/0.25$) for each 2 yr. Finally, the latitude of the convective center is defined as a meridional local minimum of raw TBB within the band from 10°N to 10°S. The total number of WIG peaks is 355 491 in 10 yr between 2000 and 2009. Figure 2c shows the WIG convective centers distributing along WIG ridges in Fig. 2b. It is seen that robust wave passages are captured while leaving weak, noisy signals are excluded.

The geographic distribution of WIG peaks is shown in Fig. 3. The WIG waves are most active in the WP and Africa, as revealed by the previous analysis (Wheeler and Kiladis 1999; Kiladis et al. 2009; Tulich and Kiladis 2012). It is noted that only peaks in the ocean are used in the composite analysis.

e. Composite analysis method

A quasi-2-day wave accompanies with an individual convective event with a period from a few hours to 1 day. Such a fast temporal variation is unable to be tracked continuously by satellite and reanalysis data owing to their coarse temporal sampling. For example, daily observation frequencies are four times (6 hourly) and less than two times in reanalysis and low-Earth-orbiting (LEO) satellite data, respectively. To circumvent this problem, Masunaga (2012) developed a new composite technique to statistically reconstruct fast temporal variations in the atmosphere, where two LEO satellite datasets are combined. In his technique, TRMM data are used to detect composite base points and the other LEO data are composited around them (his Fig. 2), where the time axis is defined as the observational time difference between the two LEO satellites. A huge number of the base points are required to obtain a statistically

continuous time series because individual composite samples only provide discrete snapshots.

A similar approach is applied to this study with major modifications. First, peaks in the filtered GEO satellite data (mergedIR) are used to detect the compositing base points as described in sections 2c and 2d. Second, various other satellites and reanalysis data are composited around the base points to construct the statistical continuous time series. Noise that happened to fall in the WIG filter (Fig. 2b) is probably included when the WIG filter is applied but would have been averaged out in the composite time series once a composite analysis is performed with a large number of the base points of the composite with a 2σ threshold to filter out weak signals.

The composite time 0 h defines the moment when WIG wave is most convectively active as implied by TBB minima. The time resolution of the composite time series is 0.5 h because the composite base points are time stamped by 0.5-hourly mergedIR data. As such, the time difference between a base point and 6-hourly ERAI is technically sorted by 0.5-hourly bins, although the composited parameters may be heavily smoothed over time.

3. Features of the composite 2-day waves

In this section, the horizontal structure and propagation character of the composite WIG waves are described. Figure 4 shows the horizontal structure of anomalous TBB, precipitation, geopotential height, and horizontal wind during a sequence of WIG phases. Anomalies represent the deviation from the temporal mean over ± 48 h in the composite time series, which are computed by subtracting the mean from the value at each grid point in Fig. 4. The computing method of anomaly is similar to that used in Takayabu et al. (1996) and Benedict and Randall (2007). Shading and arrows in

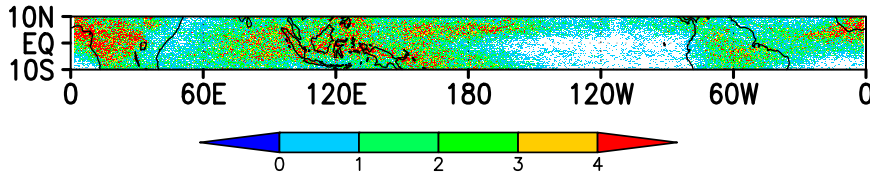


FIG. 3. Geographic distribution of WIG peaks detected by the method in section 2d. The total peak number is 355 491.

Fig. 4 are plotted only where statistically significant at the 95% level as tested by the Student's t test.

The area with a negative TBB anomaly (convective active area) has a zonal scale of about 1000 km (Fig. 4a). Therefore, the zonal wavelength of the composite WIG wave is estimated about 2000 km, corresponding to that of COARE 2-day wave (Takayabu 1994b; Takayabu et al. 1996; Haertel and Johnson 1998; Haertel and Kiladis 2004). The convective envelope moves westward with a period of about 2 days and has a minimum TBB around 0 h by definition. The TBB minimum lags the precipitation maximum by a few hours, which is consistent with the previous studies (Takayabu et al. 1996; Haertel and Johnson 1998; Haertel and Kiladis 2004). The somewhat noisy distribution of precipitation anomaly (Fig. 4b) is likely to result from the small sample size of PR2A25 data, because TRMM satellite has less than twice-daily observations at the same location. The propagation speed is estimated to be about 17 m s^{-1} given that the convective active area moves over about 30° in 48 h. It has been reported that the phase speed of quasi-2-day waves spans over a wide range from 10 to 30 m s^{-1} (Takayabu 1994b; Takayabu et al. 1996; Haertel and Johnson 1998; Haertel and Kiladis 2004). The synoptic-scale structure of geopotential height and wind at 200 hPa is reminiscent of the theoretical $n = 1$ WIG mode (Matsuno 1966) in that divergence and convergence are on the left and right, respectively, of the low pressure field [see Fig. 3 in Kiladis et al. (2009)]. The negative TBB anomaly is almost in quadrature with the geopotential height and is in phase with the wind divergence field (Wheeler et al. 2000; Haertel and Kiladis 2004; Kiladis et al. 2009).

The convective center of the composite WIG waves is shifted away from the equator to around 5°N (Fig. 4a). This could result from the effect of intertropical convergence zone, which is located near the equator (Indian Ocean; IO) and off the equator around 7°N (Pacific Ocean). In fact, the WIG convective center appears around 7°N in WP and around 0° in IO (not shown). The horizontal structure of geopotential height and wind is offset to the north of the equator (Fig. 4c), while that of theoretical $n = 1$ WIG is equatorial symmetric, probably owing to the same reason as mentioned above.

The horizontal and vertical structures are nearly identical between the Indian and Pacific Oceans (not shown). A secondary difference is that a maximum height of convection is lower in the eastern Pacific than in the Indo-western Pacific, which could be explained by the regional difference of the tropical large-scale circulation (e.g., Back and Bretherton 2006).

4. MSE budget analysis

a. Column-integrated MSE budget terms

MSE (m) is nearly conserved in moist adiabatic processes and defined as

$$s = \phi + c_p T \quad \text{and} \quad (1)$$

$$m = s + Lq, \quad (2)$$

where s is dry static energy, L is the latent heat of condensation ($2.5 \times 10^6 \text{ J kg}^{-1}$), and c_p is dry air heat capacity at constant pressure ($1004 \text{ J K}^{-1} \text{ kg}^{-1}$). The budget of column-integrated MSE is expected as follows:

$$\langle \partial_t m \rangle = -\langle \mathbf{V} \cdot \nabla m \rangle - \langle \omega \partial_p m \rangle + \langle Q_R \rangle + \text{LH} + \text{SH}. \quad (3)$$

Angle brackets represents mass-weighted vertical integration from the top of the atmosphere p_t to the surface p_s ; $\langle A \rangle = g^{-1} \int_{p_t}^{p_s} dp A$, where g is the gravitational acceleration, p_s is 1000 hPa, and p_t is 100 hPa. The left-hand side (lhs) is the MSE tendency. The first and second terms on the right-hand side (rhs) represent horizontal MSE advection (HADV) and vertical MSE advection (VADV), respectively. The other terms on rhs are MSE source terms: the radiative heating Q_R , surface latent heat flux (LH), and surface sensible heat flux (SH). The term $\langle Q_R \rangle$ is calculated as the difference in net radiative flux between the surface and top of the atmosphere:

$$\begin{aligned} \langle Q_R \rangle = & \text{SW}_t \downarrow - \text{SW}_t \uparrow - \text{SW}_s \downarrow + \text{SW}_s \uparrow \\ & - \text{LW}_t \uparrow - \text{LW}_s \downarrow + \text{LW}_s \uparrow. \end{aligned} \quad (4)$$

Upward and downward arrows represent upward and downward flux, respectively. The budget terms are computed in a square grid box with the size of 1.5° . The

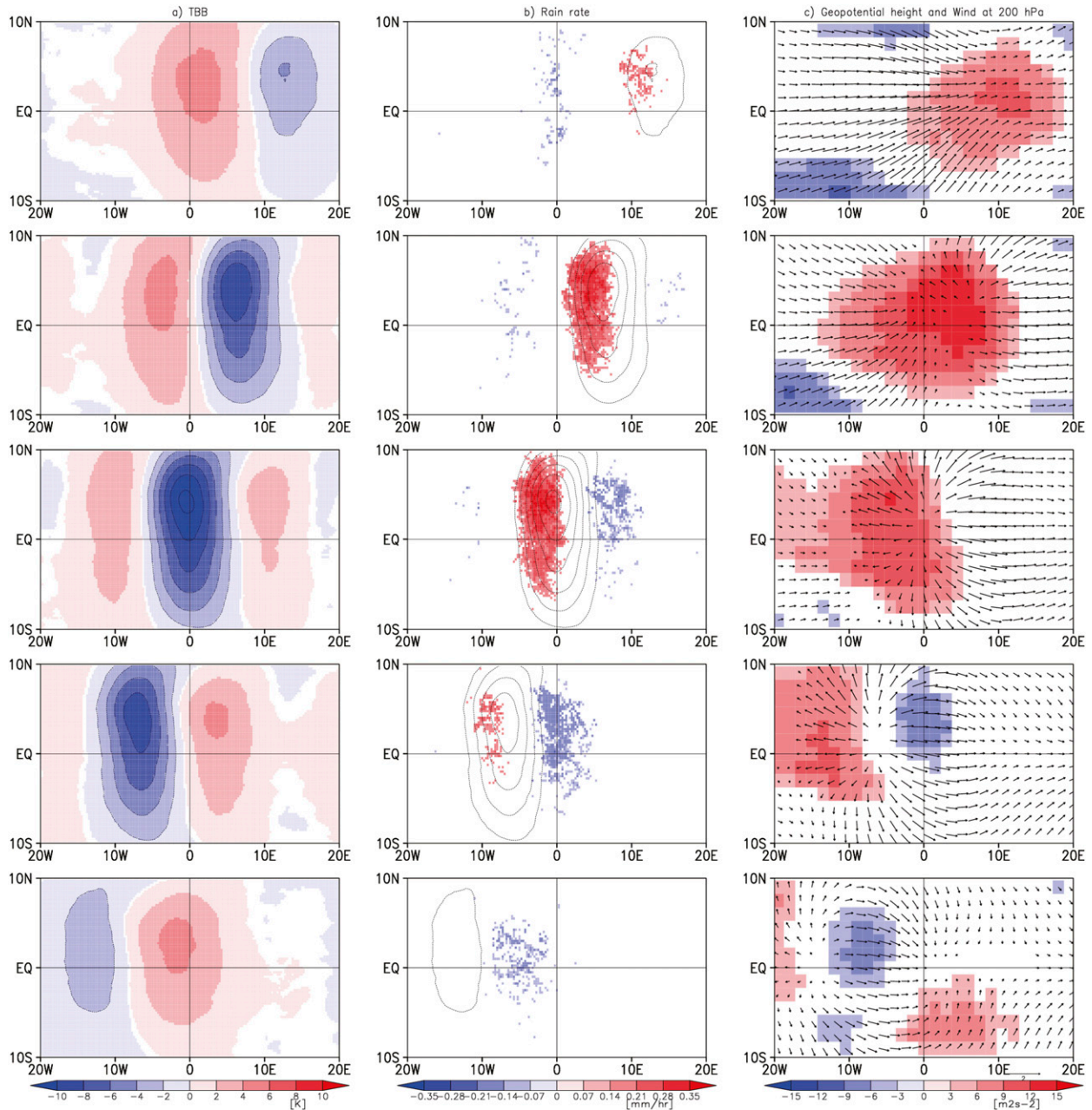


FIG. 4. 12-hourly snapshots of the horizontal structure of the composite WIG waves: (a) anomalous TBB, (b) anomalous precipitation, and (c) anomalous geopotential height (shaded) and horizontal wind (vectors) at 200 hPa. Negative anomaly of TBB is represented by contours in (a) and (b). Anomalies are computed by subtracting the time-mean value during ± 48 h in the composite time series from the values at each grid point. Shades and arrows indicate regions significant at the 95% level. The horizontal axis is a relative longitude between -20° and $+20^\circ$. The vertical axis is latitude between 10°N and 10°S . Time increases downward from -24 to $+24$ h in increments of 12 h.

box is centered on the longitude of composite center (WIG peak). Our results are insensitive to the difference in the grid size being varied between 1.5° and 7.5° .

Figure 5 shows the composite time series of the budget terms. As 6-hourly ERAI data is composited around the base points, the composite time series has wiggles every

6 h as the result of sampling inhomogeneity. The tendency term has a maximum of 100 W m^{-2} before the WIG peak (about -15 h) and a minimum of -100 W m^{-2} after the peak. This suggests that MSE increases before deep convection (MSE recharge) and decreases after convective development (MSE discharge). Total MSE

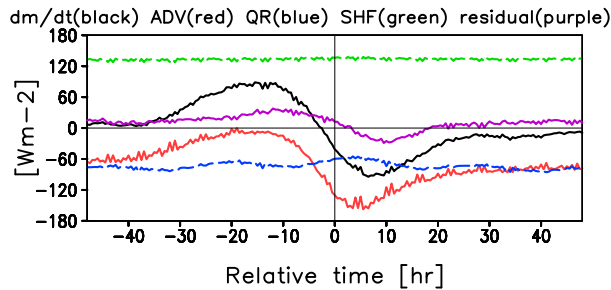


FIG. 5. Composite time series of integrated MSE budget terms: the MSE tendency (black), total MSE advection (red), surface flux (green), radiative heating (blue), and the budget residual (purple). The residual is computed by subtracting the right-hand side from the left-hand side of the budget equation.

advection term, or sum of the horizontal and vertical advectons, fluctuates between -160 and 0 W m^{-2} in phase with the tendency term. The advection increases MSE import before deep convection and approaches its maximum 0 around -15 h . Then, it drops when deep convection develops and reaches its minimum of -160 W m^{-2} after the WIG peak. Although the MSE advection shows a striking variability, the MSE source terms scarcely change with time even during active convection. Radiative and surface fluxes stay nearly constant at -60 W m^{-2} ($\text{LW} = -180 \text{ W m}^{-2}$ and $\text{SW} = +120 \text{ W m}^{-2}$) and $+130 \text{ W m}^{-2}$ ($\text{SH} = 20 \text{ W m}^{-2}$ and $\text{LH} = +110 \text{ W m}^{-2}$), respectively. The budget residual is calculated by subtracting the rhs from the lhs in Eq. (3), which fluctuates almost in phase with the tendency term. It might result from uncertainties of reanalysis data, including 1) the convection and cloud parameterizations used in the data assimilation and 2) the coarse spatiotemporal resolution. Although the budget is not closed in this analysis, the MSE recharge–discharge process is mainly regulated by the MSE advection.

Haertel et al. (2008) performed a budget analysis of integrated MSE in 2-day waves based on a two-mode model, where TOGA COARE sounding data are used as a basic state of the model. MSE source term is in opposite phase to the tendency and the amplitude is larger than our result (see their Fig. 10). Inoue and Back (2015) also showed that the surface heat flux and radiative heating are in opposite phase to the tendency in COARE 2-day wave (see their Fig. 2). Although the radiative heating in Fig. 5 is likely to be out of phase with the tendency (a maximum of the radiative heating lags the convective peak), the surface flux nearly stays constant. It is considered that MSE source terms might be underestimated in reanalysis data than in situ and satellite data, because the flux data in ERAI are provided as a time cumulative value of 6 or 12 h. In fact, column-integrated radiative heating, computed from *CloudSat* radiative flux

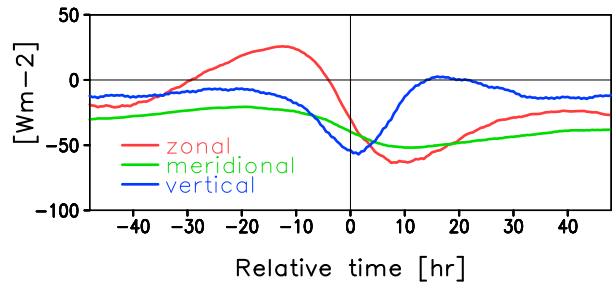


FIG. 6. As in Fig. 5, but for zonal (red), meridional (green), and vertical (blue) MSE advection.

data 2B-FLXHR-lidar (L'Ecuyer et al. 2008), has a larger amplitude of about $\pm 20 \text{ W m}^{-2}$ than ERAI data (not shown). However, such difference would not have serious effects on the present study because the amplitudes of MSE source terms are negligibly smaller than that of MSE advection during the active phase of WIG waves.

Total MSE advection is separated into the horizontal and vertical components. Figure 6 shows the composite time series of the advection terms, smoothed by moving average with temporal window of $\pm 6 \text{ h}$. The result is insensitive to changing a width of the window.

The notable change of VADV occurs mostly within $\pm 12 \text{ h}$ about the time of deep convection. An increase of negative VADV around the WIG peak corresponds to an enhancement of MSE export due to the first baroclinic mode (Peters and Bretherton 2006; Haertel et al. 2008). The previous studies also suggested that the second baroclinic mode increases positive VADV (MSE import) leading deep convection, while it is not apparent in this analysis. HADV is further separated into the zonal and meridional components: $-\langle \mathbf{V} \cdot \nabla m \rangle = -\langle u \partial_x m \rangle - \langle v \partial_y m \rangle$. Zonal advection shows a striking variability, leading to an import of MSE before the convective peak, followed by a remarkable MSE export shortly after the peak. Meridional advection with a small amplitude stays negative throughout the evolution.

Previous studies have reported that MSE recharge–discharge processes are mainly regulated by VADV in convectively coupled gravity waves. Inoue and Back (2015) showed that the MSE tendency is dominated by VADV in COARE 2-day waves and that HADV and MSE source terms are canceled out by each other. Haertel et al. (2008), based on two-mode model, showed that the recharge–discharge process in 2-day wave is mainly controlled by VADV, although they did not compute HADV directly. Using a diabatically accelerated cloud-resolving model, Peters and Bretherton (2006) showed that VADV dominate the MSE tendency both in a mesoscale convective event and a convectively coupled Kelvin wave. They also indicated that VADV is more dominant over HADV in the Kelvin wave. In this study, however, zonal

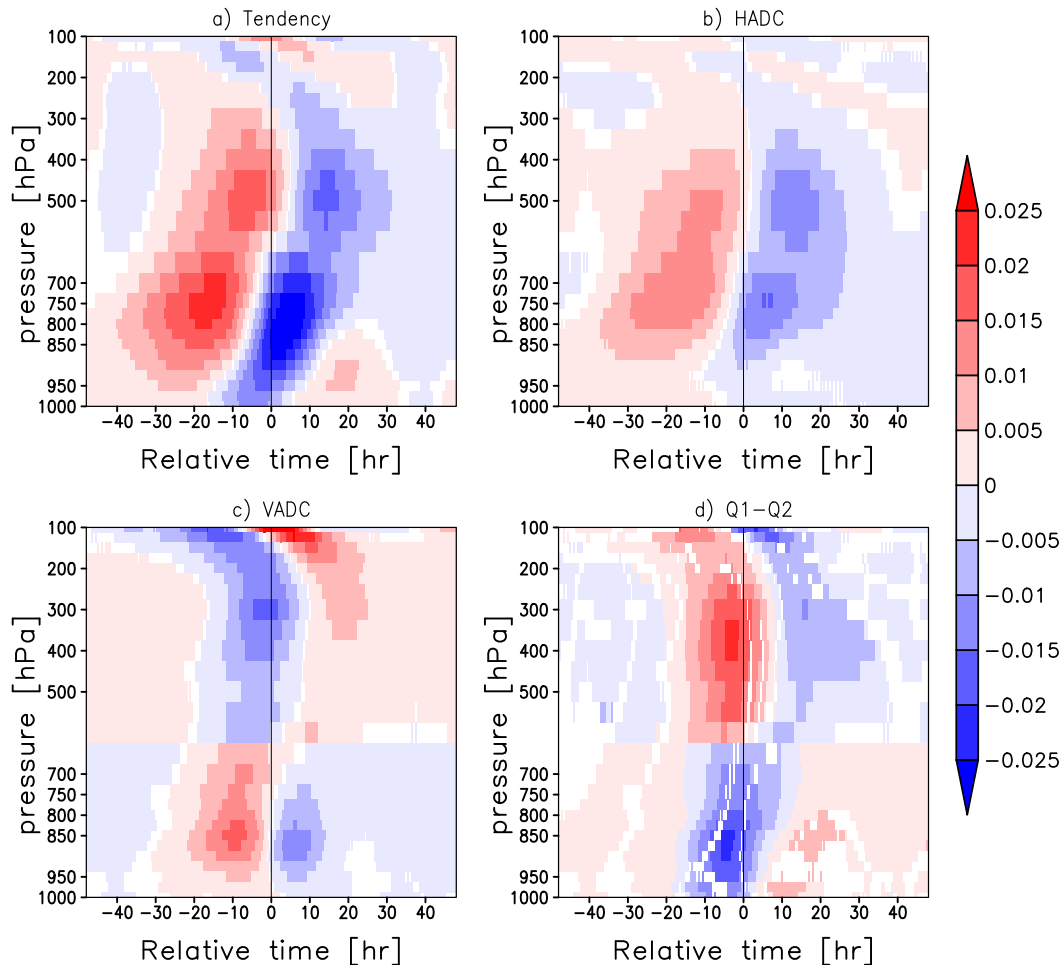


FIG. 7. Time–pressure cross sections of anomalies of the MSE budget terms ($\text{m}^2 \text{s}^{-3}$): (a) MSE tendency, (b) horizontal MSE advection, (c) vertical MSE advection, and (d) $Q_1 - Q_2$. Anomalies are computed by subtracting the time-mean value during ± 48 h in the composite time series from the values at each pressure level. Shading represents regions significant at the 95% level.

advection is as large as VADV. This result is discussed for validity in sections 4c and 4d.

b. Vertical structures of the budget terms

To analyze the vertical structure of the budget terms, we use the budget equation of MSE:

$$\partial_t m = -\mathbf{V} \cdot \nabla m - \omega \partial_p m + Q_1 - Q_2, \quad (5)$$

where Q_1 is the apparent heating source, Q_2 is moisture sink, and

$$Q_1 - Q_2 = Q_R - F_{s,ed} - LF_{q,ed}, \quad (6)$$

where MSE eddy term ($Q_1 - Q_2$) is the sum of radiative heating Q_R and MSE eddy transport ($-F_{s,ed} - LF_{q,ed}$). Eddy transport of sensible heat flux ($-F_{s,ed}$) and latent heat flux ($-LF_{q,ed}$) are not provided by reanalysis data.

Also, vertical information of Q_R is not provided in ERAI data (see section 4a). Instead of Eq. (6), $Q_1 - Q_2$ is calculated from Eq. (5) by subtracting the advection terms from the tendency term (Yanai et al. 1973). Note that the MSE eddy transport usually exceeds radiative heating in the region where deep vertical motion exists (Yanai et al. 1973), although their vertical profiles are missing in this study. In fact, Masunaga and L'Ecuyer (2014) estimated the MSE eddy transport and radiative heating from satellite data, showing that the former is much larger than the later during tropical convection with the time scale of about 1–2 days.

Figure 7 shows the time–pressure cross section of the budget terms in Eq. (5). A darker red (blue) color means a stronger MSE import (export). The tendency term vertically tilts with time and has a maximum around 750 hPa before deep convection. HADV (mainly with zonal advection) is almost in phase with the tendency

at each pressure level. Meridional advection is negligibly small as one might expect from Fig. 6 (not shown). The amplitude of VADV is comparable to that of HADV, although the variability is more confined in time to the period of intense convection between -12 and $+12$ h. Before deep convection, a positive anomaly emerges in the lower troposphere accompanied by a negative anomaly from the middle to upper troposphere (Fig. 7c). A strong updraft in the whole troposphere causes MSE increase (decrease) in the lower (upper) half of the troposphere. After WIG peak, a decrease of upper-tropospheric updraft weakens the negative VADV (positive anomaly), while an increase of lower-tropospheric downdraft enhances a negative VADV (negative anomaly). The MSE eddy term shows a prominent contribution to the budget, which is absent by definition in the column integrated terms in Fig. 5.

The vertical dipole structure of VADV could suggest that the thermodynamic process might be explained by a two-mode theory (Haertel and Kiladis 2004; Peters and Bretherton 2006; Haertel et al. 2008). During an enhancement of deep convection, the first mode causes MSE export and import in the upper and lower troposphere, respectively, leading to an increase of negative VADV (MSE discharge process). The second mode causes MSE import in the lower troposphere before deep convection, leading to an increase of positive VADV (MSE recharge process). The superposition of these modes results to a vertical tilting structure of VADV. In this study, an increase of positive VADV (Fig. 6) is much smaller than previous studies (Haertel et al. 2008; Inoue and Back 2015). A slight vertical tilt in VADV (Fig. 7) may imply the presence of a shallow updraft likely associated with the second mode leading the development of the first mode, although overwhelmed in amplitude by the first mode. This indicates that the second mode has a more minor contribution to the thermodynamic process than the first mode. The above discussion will be dealt with again in section 5c.

c. Decomposition of advection terms

Variables within advection terms are separated into the background and perturbation fields to further investigate MSE recharge–discharge process. The background is defined as the 10-yr-averaged 6-hourly climatology of ERAI data that consists of a 365-day-long time series of global maps. The perturbation represents the local deviation from the climatology. Here, zonal velocity u can be written as $u = \bar{u} + u'$, where the bar and the prime represent the background and perturbation, respectively. The zonal advection term ($-u\partial_x m$) is separated into the four components:

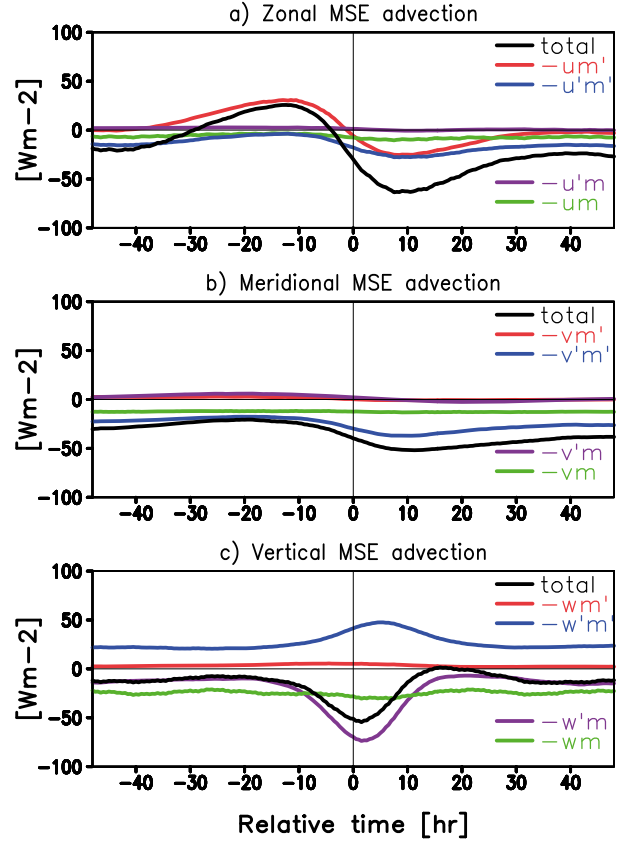


FIG. 8. As in Fig. 5, but for the MSE advection separated by the background and perturbation fields: (a) zonal, (b) meridional, and (c) vertical MSE advection. The colored lines correspond to the labeled components in the keys.

$$-u\partial_x m = -\bar{u}'\partial_x \bar{m} - u'\partial_x m' - \bar{u}\partial_x m' - \bar{u}\partial_x \bar{m}'. \quad (7)$$

The meridional and vertical advection terms are decomposed in the same way. The results are insensitive to the different definition of the background.

Figure 8 shows the composite time series of the decomposed advection terms. The background components ($-\bar{u}\partial_x \bar{m} - \bar{v}\partial_y \bar{m}$ and $-\bar{\omega}\partial_p \bar{m}$) stay small and negative (steady MSE exports). The zonal advection is largely modulated by $-\bar{u}\partial_x m'$, while $-\bar{v}\partial_y m'$ and $-\bar{\omega}\partial_p m'$ are nearly 0. Meridional advection depends on $-v'\partial_y m'$. Small amplitudes of $-u'\partial_x m'$ and $-v'\partial_y m'$ indicate that perturbation u' and v' weakly acts against m' . Vertical advection is mainly dominated by $-\omega'\partial_p \bar{m}$ involving perturbation ω' . This agrees with the previous studies indicating that VADV is associated with the large-scale vertical motion (Peters and Bretherton 2006; Haertel et al. 2008; Inoue and Back 2015).

We examine the vertical structure of the background and perturbation components included in zonal MSE advection. Figure 9 shows snapshots of the longitude–pressure

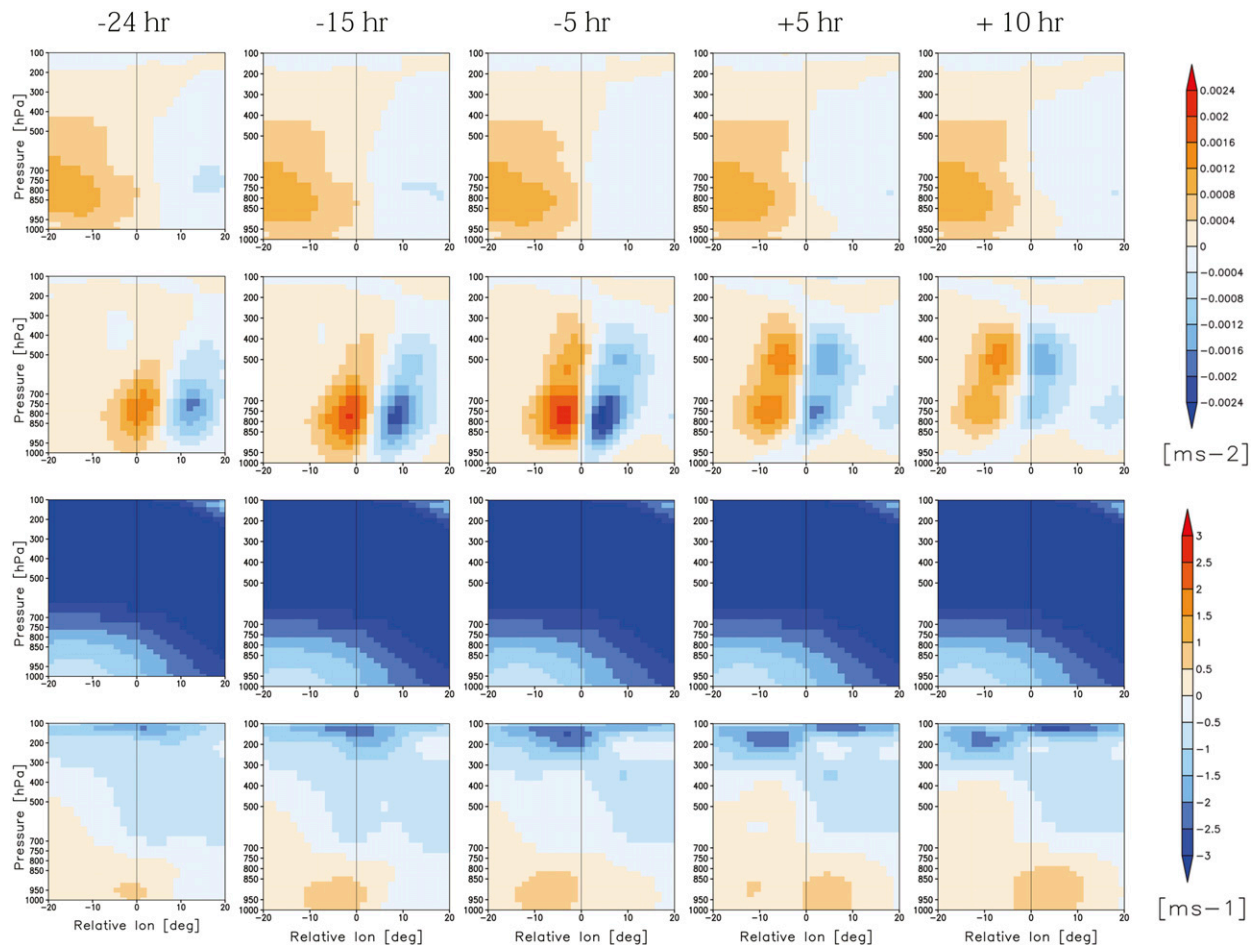


FIG. 9. Snapshots of the longitude–pressure cross sections of MSE zonal gradient (m s^{-2}) and zonal wind (m s^{-1}): $\partial_x \bar{m}$, $\partial_x m'$, \bar{u} and u' . The horizontal and vertical axes represent relative longitude and pressure, respectively. Time increases to the right ($-24, -15, -5, +5, +10$ h).

cross sections of $\partial_x \bar{m}$, $\partial_x m'$, \bar{u} , and u' . Each snapshot shows different timings from the WIG developing stages: an early stage of WIG convection (-24 h), maximum of the MSE tendency (-15 h), near-precipitation maximum (-5 h), minimum of the MSE tendency ($+5$ h), and a decaying stage of WIG convection ($+10$ h). The zonal gradient of the background MSE $\partial_x \bar{m}$ has a small negative and a large positive value to the east and the west of the origin, respectively. The perturbation MSE gradient $\partial_x m'$ is larger than $\partial_x \bar{m}$ and is positive and negative on the west and the east of m' , respectively. An eastward tilting of $\partial_x m'$ represents that the perturbation MSE m' tilts eastward (not shown). The background zonal wind \bar{u} is easterly ($\sim 5 \text{ m s}^{-1}$) everywhere from the surface to the tropopause, which is slower than the propagation speed of the composite WIG wave ($\sim 17 \text{ m s}^{-1}$). This implies that a synoptic-scale convective system accompanied with WIG waves could not be driven westward by the background easterly wind. The perturbation wind u' is large in amplitudes near the tropopause, which is a well-

known character of 2-day waves (Takayabu et al. 1996; Haertel and Johnson 1998; Haertel and Kiladis 2004). Overall, \bar{u} constantly overwhelms u' in magnitude and $\partial_x m'$ shows a more distinct variability than $\partial_x \bar{m}$, which leads to a striking value of $-\bar{u} \partial_x m'$ as will be seen below.

Figure 10 shows the longitude–pressure cross sections of decomposed zonal MSE advection. The zonal advection $-u \partial_x m$ is dominated by $-\bar{u} \partial_x m'$ in the free troposphere, while the other components are less prominent as expected from Fig. 8. The term $-\bar{u} \partial_x m'$ has the same dipole structure as $\partial_x m'$. Because \bar{u} is predominantly easterly in the free troposphere (Fig. 9), $-\bar{u} \partial_x m'$ generates MSE increase to the west of a positive m' and MSE decrease to the east of it. In the next section, we compare MSE recharge–discharge processes in different background zonal wind to verify the above scenario.

d. Zonal wind effect

To examine the possible roles of the background zonal wind on the MSE budget, we define a barotropic flow

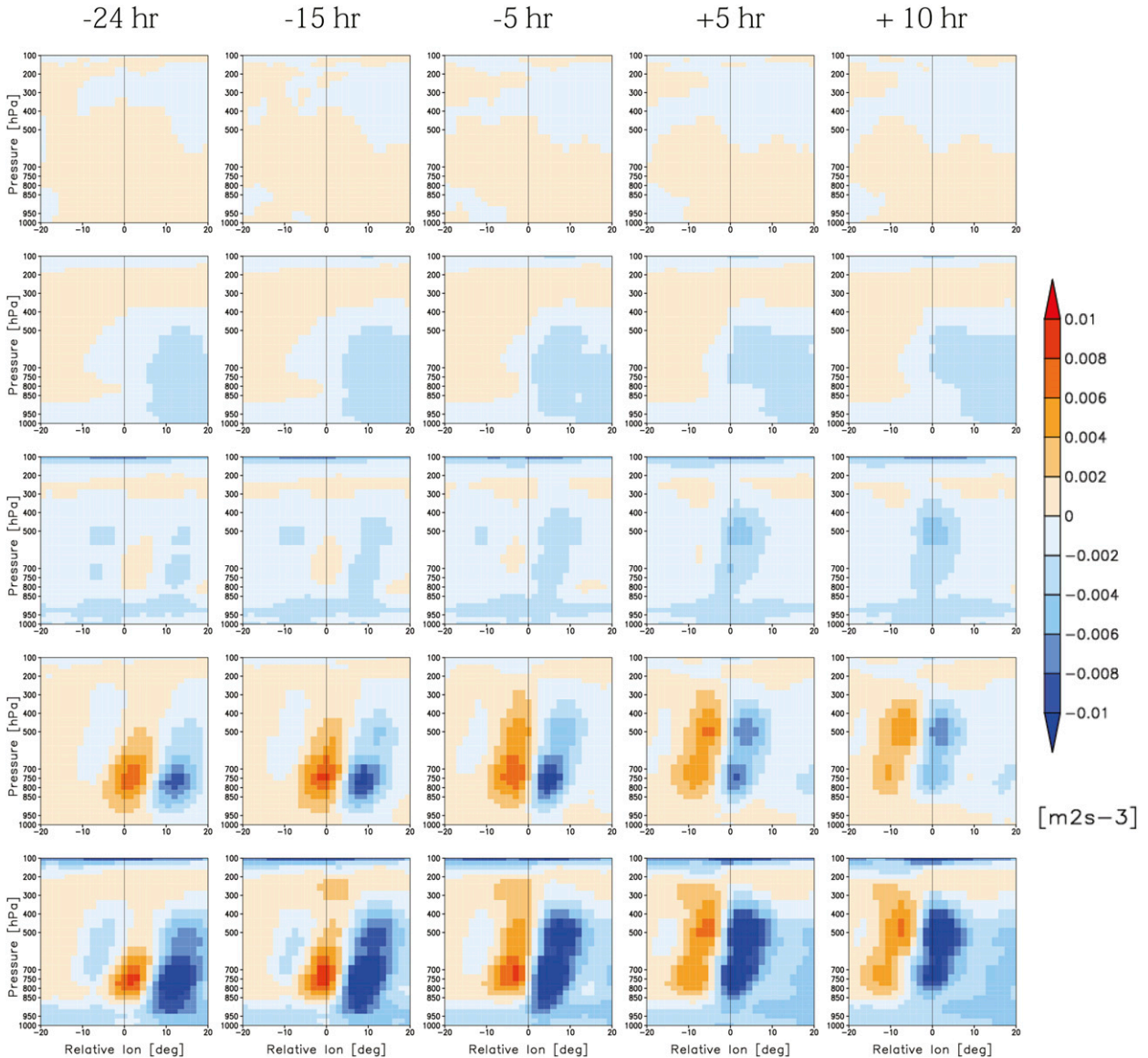


FIG. 10. As in Fig. 9, but for the four components of zonal MSE advection decomposed by the background and perturbation fields: $-u'\partial_x \bar{m}$, $-\bar{u}\partial_x \bar{m}$, $-u'\partial_x m'$, $-\bar{u}\partial_x m'$, and $-u\partial_x m$ ($\text{m}^2 \text{s}^{-3}$).

as a vertically averaged \bar{u} between 700 and 800 hPa, where the tendency and MSE advection have striking variabilities (see Fig. 7). The base points of composite (WIG peaks) are categorized into five groups by the barotropic flow at location of the points as shown in Table 1. Categories C1 and C5 correspond to the strongest easterly and westerly flow, respectively. Each of C1–C4 includes about 20%–25% and C5 includes about 8%.

Figure 11 shows the composite time series of anomalous MSE tendency, HADV, and VADV for different barotropic flow. The anomaly is the deviation from the temporal mean over ± 48 h during the composite time series. Whenever the background barotropic flow is

easterly (C1–C3) or westerly (C4–C5), the tendency and HADV are in phase with each other. As the barotropic easterly flow becomes stronger, their amplitudes become larger owing to $-\bar{u}\partial_x m'$. Meanwhile, VADV is insensitive to the direction and magnitude of the background wind speed. In the easterly flow, $-\bar{u}\partial_x m'$ and $-u'\partial_x m'$ are in phase with each other (see Fig. 8), leading to a large amplitude of HADV (e.g., C1 in Fig. 11). Although $-u'\partial_x m'$ is identical to that in the easterly flow, it is out of phase with $-\bar{u}\partial_x m'$ in the westerly flow (not shown), canceling each other out in HADV (e.g., C5 in Fig. 11).

The coherence of $-\bar{u}\partial_x m'$ with the MSE tendency implies that this term is largely left unconsumed during

TABLE 1. Category of barotropic flow between 700 and 800 hPa.

Category	Barotropic flow (m s^{-1})	Percentile
C1	≤ -5.7	0 to 26
C2	-5.4 to -3.0	26 to 52
C3	-2.7 to 0.0	52 to 72
C4	0.3 to 3.9	72 to 92
C5	≥ 4.2	92 to 100

a passage of the WIG wave and thus is not critical of 2-day wave dynamics. As \bar{u} is slower than the wave propagation speed of about 17 m s^{-1} , the term $-\bar{u}\partial_x m'$ brings an MSE anomaly from the near side of the WIG peak itself. Under the easterly background, this results in a positive MSE advection because the near side lies ahead of the convective peak where the lower troposphere is moist. When the background is westerly, in contrast, the horizontal MSE advection feels a dry anomaly behind the wave peak and counteracts the moistening due to the wave itself, which is primarily regulated by the vertical advection.

e. Gross moist stability

The MSE recharge–discharge process in WIG waves is dominated by the vertical advection associated with a large-scale circulation. Here, GMS is adopted to investigate the convective–wave coupling mechanism. Neelin and Held (1987) first introduced GMS as a tool to simplify the relationship between moist convection and large atmospheric circulations. In their two-dimensional model, GMS was a time invariant parameter and was meaningful only when GMS is positive because otherwise the system would be unstable and time dependent.

Recently, GMS has been tested in much broader contexts including the so-called normalized GMS (NGMS) (Raymond and Fuchs 2007; Raymond et al. 2009; Sessions et al. 2010; Kuang 2011; Hannah and Maloney 2011; Andersen and Kuang 2012; Benedict et al. 2014; Sobel et al. 2014). For example, Raymond et al. (2009) defined NGMS as “the ratio of net lateral outflow of MSE from an atmospheric column to some measure of convective intensity within the column.” The sign and magnitude of NGMS are a measure to characterize how convective heating and large-scale dynamics work together. Utilizing the definition of NGMS in Raymond et al. (2009), we examine the roles of convection in the large-scale dynamics associated with WIG waves. NGMS is defined as

$$\text{NGMS} = -\frac{\langle \omega \partial_p m \rangle}{-L \langle \omega \partial_p q \rangle}, \quad (8)$$

where the denominator is moisture vertical advection and numerator is MSE vertical advection. Unlike Raymond et al. (2009), only VADV is included in the numerator,

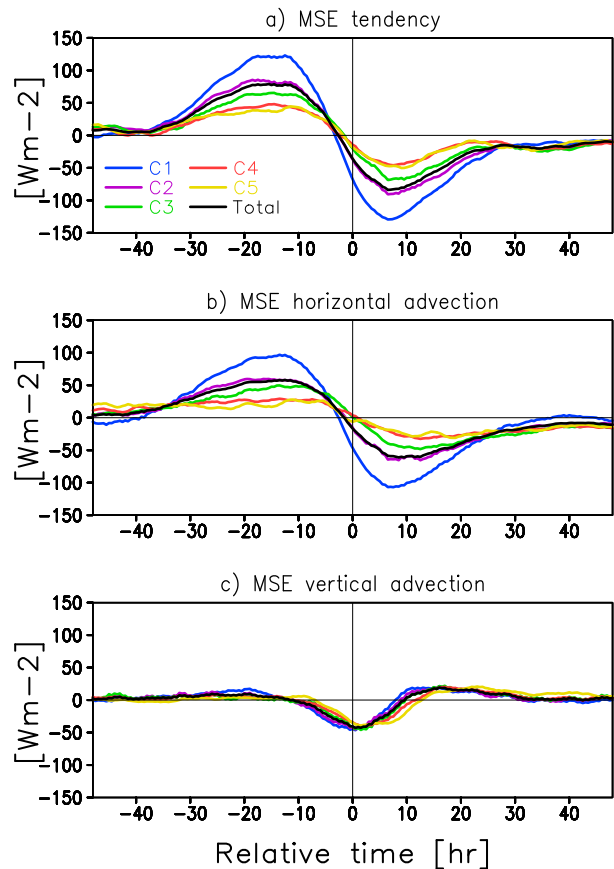


FIG. 11. As in Fig. 5, but for (a) MSE tendency, (b) horizontal MSE advection, and (c) vertical MSE advection. The WIG peaks are categorized by the background barotropic flow between 700 and 800 hPa (see Table 1). Categories C1 (blue), C2 (purple), and C3 (green) represent easterly flow, and C4 (red) and C5 (yellow) represent westerly flow.

because it is an inherent driver of the recharge–discharge process in WIG waves as presented in sections 4c and 4d.

Figure 12a shows the composite time series of the denominator and numerator in Eq. (8). The noise is smoothed out by applying a ± 6 -h moving average. The result is insensitive to the smoothing. The sign of NGMS reflects that of VADV because the vertical moisture advection is always positive (moisture import). Figure 12b shows that NGMS decreases gradually before deep convection and approaches 0 around -20 h when VADV is nearly 0. NGMS increases as deep convection passes its peak and arrives at its maximum 0.2 around $+6$ h.

Masunaga and L’Ecuyer (2014) calculated the similar composite time series of NGMS from satellite observations of tropical convection, varying with time on an hourly to daily time scale for the horizontal scale of about 100 km. Although their analysis was not targeted on any particular wave mode, NGMS decreases toward 0 before deep convection and increases following

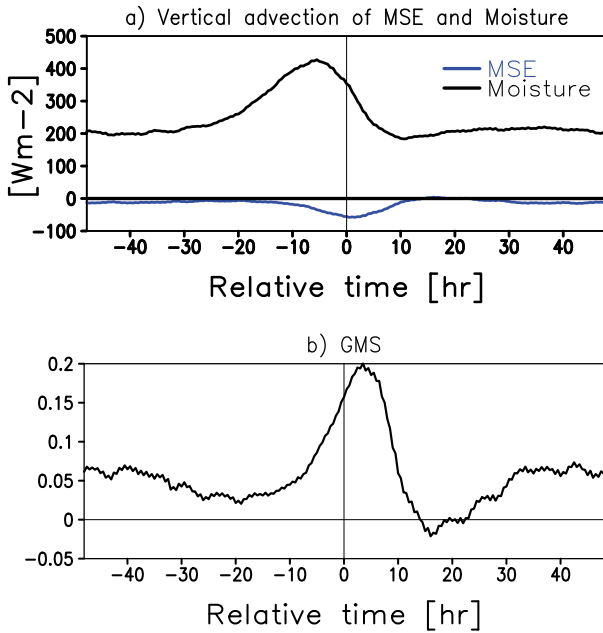


FIG. 12. As in Fig. 5, but for (a) vertical MSE advection (blue) and vertical moisture advection (black) and (b) normalized GMS.

convection development, closely resembling Fig. 12b. Moisture and MSE convergence are largely controlled by vertical advection in Masunaga and L’Ecuyer (2014). The large contribution of VADV might be because the horizontal scale of the convection in their analysis is much smaller than that in the composite WIG waves (Fig. 4). Also, it is possible that the contribution of the second baroclinic mode is underestimated in ERAI data. In section 5b, we will discuss again why the contribution of the second mode is smaller in this study than in previous studies (Haertel et al. 2008; Inoue and Back 2015).

Figure 13 shows the zonal distribution of precipitation and NGMS. The area of active precipitation with the zonal scale of about 1000 km moves westward as expected from Fig. 4. Convective rainfall peaks a few hours earlier than stratiform rainfall in ± 5 h, which is a well-known property of tropospheric mesoscale convective systems (Houze 2004). NGMS has a significantly high value to the east of the precipitation peak. NGMS has a lower value to the west of the peak, in which VADV closes to 0. This might suggest that an area favorable (unfavorable) for the development of convection emerges to the west (east) of the convective envelope.

5. Discussion

a. Comparison with the other CCEWs and MJO

In convectively coupled gravity waves, HADV is known to be less important than VADV to controlling

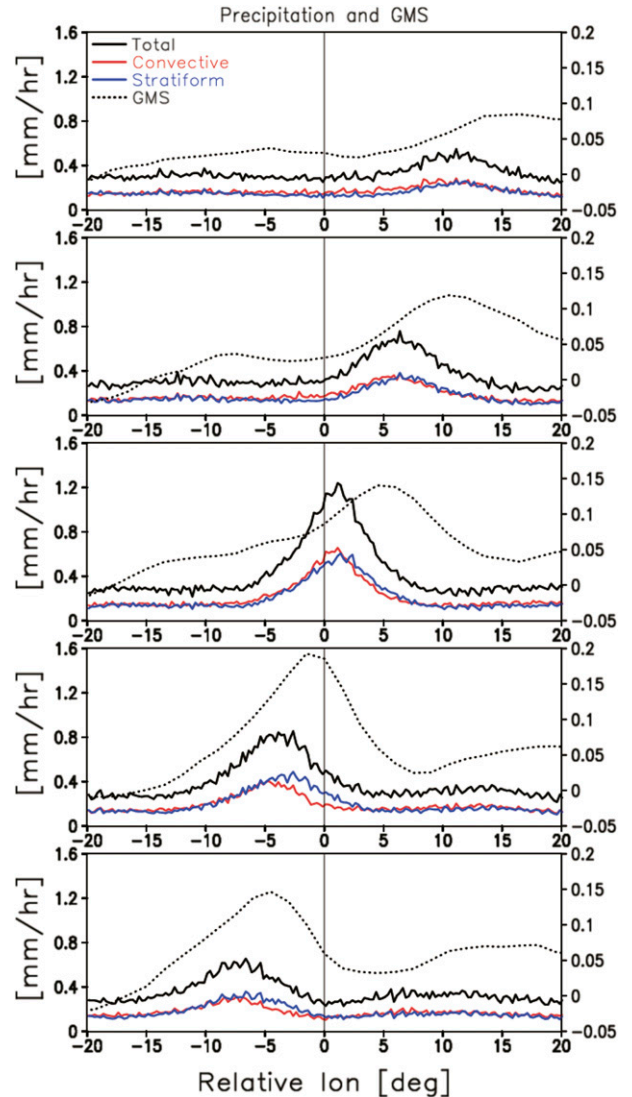


FIG. 13. Snapshots of zonal distribution of precipitation and GMS. Solid lines represent total (black), convective (red), and stratiform (blue) rainfall rate. Dotted line represents normalized GMS. The horizontal axis is the relative longitude between -20° and $+20^\circ$. (top)–(bottom) The time increases from -24 , -15 , -5 , $+5$, $+10$ h.

a MSE recharge–discharge process. Peters and Bretherton (2006), based on a cloud-resolving model, showed that VADV is dominant over HADV in the Kelvin wave. Haertel et al. (2008) and Inoue and Back (2015) showed that a column MSE is mainly controlled by VADV in COARE 2-day waves (WIG waves). The results in this study also support the previous studies, indicating that VADV plays a primary role in maintaining the thermodynamic process. However, HADV in Fig. 5 is larger than that in the COARE 2-day wave (Inoue and Back 2015). This discrepancy could be

explained by the difference of the background zonal wind. In the present study, $-\bar{u}\partial_x m'$ and $-u'\partial_x m'$ are in phase because of background easterly wind (see Fig. 9), leading to an emphasis of HADV. Meanwhile, the background zonal wind is strong westerly in the lower troposphere during TOGA COARE IOP (Chen et al. 1996; Ciesielski et al. 1997; Yanai et al. 2000). HADV in COARE 2-day wave could be weakened because $-\bar{u}\partial_x m'$ and $-u'\partial_x m'$ are opposite in phase under the background westerly (see also section 4d).

In MJO, both VADV and HADV are responsible for the MSE recharge–discharge process. HADV could play an important role in the eastward-propagation mechanism of the MJO (Maloney 2009; Maloney et al. 2010; Kiranmayi and Maloney 2011; Benedict et al. 2014; Kim et al. 2014; Sobel et al. 2014). As noted in the previous paragraph, an importance of HADV is small in the WIG wave and Kelvin wave. This corresponds to the result in Inoue and Back (2015) showing that a relative contribution of HADV increases as the time scale of the disturbance grows to intraseasonal scales.

There are some differences in the thermodynamic process of the MJO compared to the WIG wave. First, MSE source terms have the same amplitude as the MSE advection and play an important role in regulating a column MSE. Also, radiative and surface fluxes fluctuate larger as the time scale of the disturbance becomes longer (e.g., Inoue and Back 2015). Second, the meridional advection has a striking variability during the MJO propagation. Third, the perturbation wind (u' and v'), associated with the wave kinetics, causes equal or larger MSE advection than the background wind (\bar{u} and \bar{v}). Meanwhile, eddy MSE advection ($-u'\partial_x m'$ and $-v'\partial_y m'$) stays small in WIG waves. This difference may be because the variation of environmental fields changes with the spatiotemporal scale of CCEWs (Kiladis et al. 2009). For example, the amplitude of u' in WIG is about 10% of that in MJO (Benedict and Randall 2007; Haertel et al. 2008; Kiladis et al. 2009).

b. Comparison with two-mode model

The two-mode model well captured MSE recharge–discharge processes in the convectively coupled gravity waves (Peters and Bretherton 2006; Haertel et al. 2008). The shallow vertical motion with the second baroclinic mode causes a positive VADV preceding deep convection (MSE recharge process). The strong vertical motion associated with the first baroclinic mode causes a negative VADV (MSE discharge process). After the convective peak, the descending motion in the lower troposphere and the ascending motion in the upper troposphere with the second mode cause a negative VADV (MSE discharge process). Also, previous studies have emphasized

a prominent contribution of the second mode in the 2-day wave dynamics. Haertel and Kiladis (2004), based on a two-dimensional inviscid primitive equation linearized about a basic state, showed that the wave dynamics and structure are well described by a superposition of the first and second modes. Yasunaga and Mapes (2012a) and Yasunaga and Mapes (2014) showed a significant coherence between rain and midtroposphere divergence in WIG waves, suggesting an importance of the second mode to the wave dynamics.

The framework of the two-mode model could be applied to this study. In Fig. 6, a negative VADV around a WIG peak might be explained by the first mode. A positive VADV with the second mode is not visually evident, although a slight vertical tilt provides a hint of the second mode (Fig. 7). The lack of a clear signature of shallow moistening by the congestus mode (Peters and Bretherton 2006; Haertel et al. 2008) might be a unique feature of WIG waves or possibly due to the technical limitation in reproducing a shallow updraft in reanalysis data. It could be difficult for reanalysis data to resolve a rapid variation associated with shallow circulation owing to the coarse resolution. Despite an obscure contribution of the second mode, this study hardly denies a primary importance of the second baroclinic mode in the wave dynamics. It would be beneficial elsewhere to test carefully to what extent a premoistening of the second mode is important in the WIG wave dynamics in comparison with the vertical mode decomposition technique used in recent investigations (Handlos and Back 2014; Masunaga and L'Ecuyer 2014).

c. Westward-propagation mechanism of 2-day waves

Previous studies based on ground and satellite measurements showed that most of the convective systems accompanied with 2-day waves move westward (Takayabu 1994b; Takayabu et al. 1996; Chen and Houze 1997; Haertel and Johnson 1998; Haertel and Kiladis 2004). It is outside the scope of this study to explore the origins of westward propagation because the 2-day wave is currently extracted by a WIG filter and by design moves westward. Nevertheless, a brief discussion on the selection of propagation direction in the general context might be beneficial.

Here, the propagation dynamics is examined in terms of thermodynamic process. As the low (high)-NGMS area exists to the west (east) of preexisting convection, new convection prefers to arise to the west of the preexisting convection. Hence, a synoptic-scale convective system accompanied with the WIG wave could move westward. This dynamics mainly depend on the generic properties of inertia–gravity waves, and the same dynamics with opposite signs would presumably help

convection move eastward when coupled with the eastward inertia–gravity (EIG) waves.

The present analysis presents no clear evidence that the background state plays roles in breaking the east–west symmetry in the propagation direction. Recently, [Tulich and Kiladis \(2012\)](#), using the Weather Research and Forecast (WRF) Model, indicated that the zonal wind shear in the lower troposphere is important to westward propagation of 2-day wave. Key parameters responsible for the propagation characteristics of 2-day waves will be addressed in more depth in the future.

d. Phase speed

As shown in [section 4](#), the thermodynamic process is mainly regulated by a large-scale vertical circulation and might not depend on the background zonal wind speed. Meanwhile, a further analysis is needed to discuss the relationship between the wave propagation dynamics and the background wind (e.g., [Tulich and Kiladis 2012](#)). Previous studies have discussed in various detail the WIG phase speed, which is slower than the theoretically expected one. In the vertical mode perspective, [Haertel and Kiladis \(2004\)](#) showed that the shallow equivalent depth could result from a superposition of the first and second baroclinic modes. The first baroclinic theory explained the phase speed of CCEWs by a constant GMS ([Emanuel et al. 1994](#); [Neelin and Yu 1994](#); [Raymond et al. 2009](#)). Based on a cross-spectral analysis, [Yasunaga and Mapes \(2012a\)](#) and [Yasunaga and Mapes \(2014\)](#) showed that the fast and slow WIG waves have different moist processes. [Takayabu \(1994b\)](#) and [Dias and Kiladis \(2014\)](#) reported Doppler shifting by the background zonal wind in WIG waves. Furthermore, [Dias and Kiladis \(2014\)](#) showed that the equivalent depth is uniform between the different climatological regions if the Doppler shifting is considered. It is still unclear, however, how the phase speed of the WIG wave is modified by the background zonal wind and the moist process. To approach the above problem, in a future study we will calculate the first and second baroclinic mode adequately in the different background field and estimate their modifications to the phase speed.

6. Summary

The present study explores the driving mechanism of quasi-2-day waves with a focus on the underlying thermodynamic processes. Satellite and reanalysis data are utilized for analyzing the MSE budget of convectively coupled WIG waves, which is considered to account for quasi-2-day waves to the extent that the synoptic-scale structure is approximated by linear dry dynamics. WIG waves are detected by a filtering analysis of brightness

temperature (mergedIR). The budget terms calculated from the reanalysis data (ERA-Interim) are composited around the WIG peaks to create statistically continuous time series. The horizontal dynamic structure of composite WIG waves is confirmed to be overall as expected from previous studies.

MSE advection mainly regulates MSE variability. Meanwhile, surface fluxes and radiative heating bring about nearly constant MSE import and export, respectively, and hardly contribute the wave variability throughout the evolution. An enhancement of negative vertical advection decreases column MSE around WIG peak, plausibly resulting from the first baroclinic mode developed in association with deep convection. Zonal MSE advection causes a significant MSE increase and a decrease before and after deep convection, respectively, overwhelming vertical advection in magnitude. The zonal advection is mainly dominated by $-\bar{u}\partial_x m'$, while the term should be considered separately to the MSE recharge–discharge process. It is implied that vertical advection rather than horizontal advection modulates the thermodynamic process in the WIG waves. This result is consistent with the previous studies explaining the recharge–discharge process by a large-scale vertical circulation ([Peters and Bretherton 2006](#); [Haertel et al. 2008](#); [Inoue and Back 2015](#)). A slight contribution of the second baroclinic mode in this study might result from the technical limitation in reproducing a shallow updraft in reanalysis data.

NGMS is used to examine thermodynamic processes involving the large-scale dynamics and convective heating. Before deep convection, NGMS gradually decreases from a positive value to a significant small positive value near 0. According to the development of deep convection, NGMS increases and reaches its maximum after the WIG peak. The results suggest that the low (high) NGMS leads to (lags) deep convection. In the convective envelope associated with WIG waves, new convection is allowed to develop to the west of the pre-existing convection where NGMS decreases toward zero.

The results obtained in the present study are nearly consistent with the previous investigations based on the two-mode theory, although the second baroclinic mode is invisible in this analysis. Ongoing work is testing carefully to what extent a premoistening of the second mode works in the WIG wave dynamics.

Acknowledgments. The authors thank Dr. Dave Raymond for the meaningful discussion and his insightful comments. The authors also thank Dr. George Kiladis and one anonymous reviewer for their helpful comments and suggestions, which improved this manuscript. The global-merged IR brightness temperature

data were provided by the National Centers for Environmental Prediction (NCEP) Climate Prediction Center (CPC). The TRMM PR (2A25) datasets were provided by the Japan Aerospace Exploration Agency (JAXA). ECMWF ERA-Interim data were provided by ECMWF. This work is partly supported by the Japan Society for the Promotion of Science (JSPS) Grant-in-Aid (KAKENHI) for Scientific Research (B) (26287113).

REFERENCES

- Andersen, J. A., and Z. Kuang, 2012: Moist static energy budget of MJO-like disturbances in the atmosphere of a zonally symmetric aquaplanet. *J. Climate*, **25**, 2782–2804, doi:10.1175/JCLI-D-11-00168.1.
- Back, L. E., and C. S. Bretherton, 2006: Geographic variability in the export of moist static energy and vertical motion profiles in the tropical Pacific. *Geophys. Res. Lett.*, **33**, L17810, doi:10.1029/2006GL026672.
- Benedict, J. J., and D. A. Randall, 2007: Observed characteristics of the MJO relative to maximum rainfall. *J. Atmos. Sci.*, **64**, 2332–2354, doi:10.1175/JAS3968.1.
- , E. D. Maloney, A. H. Sobel, and D. M. Frierson, 2014: Gross moist stability and MJO simulation skill in three full-physics GCMs. *J. Atmos. Sci.*, **71**, 3327–3349, doi:10.1175/JAS-D-13-0240.1.
- Bretherton, C. S., M. E. Peters, and L. E. Back, 2004: Relationships between water vapor path and precipitation over the tropical oceans. *J. Climate*, **17**, 1517–1528, doi:10.1175/1520-0442(2004)017<1517:RBWVPA>2.0.CO;2.
- Chen, S. S., and R. A. Houze, 1997: Diurnal variation and life-cycle of deep convective systems over the tropical Pacific warm pool. *Quart. J. Roy. Meteor. Soc.*, **123**, 357–388, doi:10.1002/qj.49712353806.
- , —, and B. E. Mapes, 1996: Multiscale variability of deep convection in relation to large-scale circulation in TOGA COARE. *J. Atmos. Sci.*, **53**, 1380–1409, doi:10.1175/1520-0469(1996)053<1380:MVODCI>2.0.CO;2.
- Ciesielski, P. E., L. M. Hartten, and R. H. Johnson, 1997: Impacts of merging profiler and rawinsonde winds on TOGA COARE analyses. *J. Atmos. Oceanic Technol.*, **14**, 1264–1279, doi:10.1175/1520-0426(1997)014<1264:IOMPAR>2.0.CO;2.
- Dias, J., and G. N. Kiladis, 2014: Influence of the basic state zonal flow on convectively coupled equatorial waves. *Geophys. Res. Lett.*, **41**, 6904–6913, doi:10.1002/2014GL061476.
- Emanuel, K. A., J. David Neelin, and C. S. Bretherton, 1994: On large-scale circulations in convecting atmospheres. *Quart. J. Roy. Meteor. Soc.*, **120**, 1111–1143, doi:10.1002/qj.49712051902.
- Fuchs, Ž., and D. J. Raymond, 2007: A simple, vertically resolved model of tropical disturbances with a humidity closure. *Tellus*, **59A**, 344–354, doi:10.1111/j.1600-0870.2007.00230.x.
- Haertel, P. T., and R. H. Johnson, 1998: Two-day disturbances in the equatorial western Pacific. *Quart. J. Roy. Meteor. Soc.*, **124**, 615–636, doi:10.1002/qj.49712454611.
- , and G. N. Kiladis, 2004: Dynamics of 2-day equatorial waves. *J. Atmos. Sci.*, **61**, 2707–2721, doi:10.1175/JAS3352.1.
- , —, A. Denno, and T. M. Rickenbach, 2008: Vertical-mode decompositions of 2-day waves and the Madden–Julian oscillation. *J. Atmos. Sci.*, **65**, 813–833, doi:10.1175/2007JAS2314.1.
- Handlos, Z. J., and L. E. Back, 2014: Estimating vertical motion profile shape within tropical weather states over the oceans. *J. Climate*, **27**, 7667–7686, doi:10.1175/JCLI-D-13-00602.1.
- Hannah, W. M., and E. D. Maloney, 2011: The role of moisture–convection feedbacks in simulating the Madden–Julian oscillation. *J. Climate*, **24**, 2754–2770, doi:10.1175/2011JCLI3803.1.
- Holloway, C. E., and J. D. Neelin, 2009: Moisture vertical structure, column water vapor, and tropical deep convection. *J. Atmos. Sci.*, **66**, 1665–1683, doi:10.1175/2008JAS2806.1.
- Houze, R. A., 2004: Mesoscale convective systems. *Rev. Geophys.*, **42**, 4003, doi:10.1029/2004RG000150.
- Iguchi, T., T. Kozu, R. Meneghini, J. Awaka, and K. Okamoto, 2000: Rain-profiling algorithm for the TRMM precipitation radar. *J. Appl. Meteor.*, **39**, 2038–2052, doi:10.1175/1520-0450(2001)040<2038:RPAFTT>2.0.CO;2.
- Inoue, K., and L. Back, 2015: Column-integrated moist static energy budget analysis on various time scales during TOGA COARE. *J. Atmos. Sci.*, **72**, 1856–1871, doi:10.1175/JAS-D-14-0249.1.
- Janowiak, J. E., R. J. Joyce, and Y. Yarosh, 2001: A real-time global half-hourly pixel-resolution infrared dataset and its applications. *Bull. Amer. Meteor. Soc.*, **82**, 205–217, doi:10.1175/1520-0477(2001)082<0205:ARTGHH>2.3.CO;2.
- Kalnay, E., and Coauthors, 1996: The NCEP/NCAR 40-Year Reanalysis Project. *Bull. Amer. Meteor. Soc.*, **77**, 437–471, doi:10.1175/1520-0477(1996)077<0437:TNYRP>2.0.CO;2.
- Kikuchi, K., 2014: An introduction to combined Fourier–wavelet transform and its application to convectively coupled equatorial waves. *Climate Dyn.*, **43**, 1339–1356, doi:10.1007/s00382-013-1949-8.
- , and Y. N. Takayabu, 2004: The development of organized convection associated with the MJO during TOGA COARE IOP: Trimodal characteristics. *Geophys. Res. Lett.*, **31**, L10101, doi:10.1029/2004GL019601.
- Kiladis, G. N., C. D. Thorncroft, and N. M. Hall, 2006: Three-dimensional structure and dynamics of African easterly waves. Part I: Observations. *J. Atmos. Sci.*, **63**, 2212–2230, doi:10.1175/JAS3741.1.
- , M. C. Wheeler, P. T. Haertel, K. H. Straub, and P. E. Roundy, 2009: Convectively coupled equatorial waves. *Rev. Geophys.*, **47**, 2003, doi:10.1029/2008RG000266.
- Kim, D., J.-S. Kug, and A. H. Sobel, 2014: Propagating versus nonpropagating Madden–Julian oscillation events. *J. Climate*, **27**, 111–125, doi:10.1175/JCLI-D-13-00084.1.
- Kiranmayi, L., and E. D. Maloney, 2011: Intraseasonal moist static energy budget in reanalysis data. *J. Geophys. Res.*, **116**, D21117, doi:10.1029/2011JD016031.
- Kuang, Z., 2008: A moisture–stratiform instability for convectively coupled waves. *J. Atmos. Sci.*, **65**, 834–854, doi:10.1175/2007JAS2444.1.
- , 2011: The wavelength dependence of the gross moist stability and the scale selection in the instability of column-integrated moist static energy. *J. Atmos. Sci.*, **68**, 61–74, doi:10.1175/2010JAS3591.1.
- L’Ecuyer, T. S., N. B. Wood, T. Haladay, G. L. Stephens, and P. W. Stackhouse, 2008: Impact of clouds on atmospheric heating based on the R04 CloudSat fluxes and heating rates data set. *J. Geophys. Res.*, **113**, D00A15, doi:10.1029/2008JD009951.
- Maloney, E. D., 2009: The moist static energy budget of a composite tropical intraseasonal oscillation in a climate model. *J. Climate*, **22**, 711–729, doi:10.1175/2008JCLI2542.1.
- , A. H. Sobel, and W. M. Hannah, 2010: Intraseasonal variability in an aquaplanet general circulation model. *J. Adv. Model. Earth Syst.*, **2** (5), doi:10.3894/JAMES.2010.2.5.
- Mapes, B. E., 2000: Convective inhibition, subgrid-scale triggering energy, and stratiform instability in a toy tropical

- wave model. *J. Atmos. Sci.*, **57**, 1515–1535, doi:10.1175/1520-0469(2000)057<1515:CISSTE>2.0.CO;2.
- , S. Tulich, J. Lin, and P. Zuidema, 2006: The mesoscale convection life cycle: Building block or prototype for large-scale tropical waves? *Dyn. Atmos. Oceans*, **42**, 3–29, doi:10.1016/j.dynatmoce.2006.03.003.
- Masunaga, H., 2007: Seasonality and regionality of the Madden-Julian oscillation, Kelvin wave, and equatorial Rossby wave. *J. Atmos. Sci.*, **64**, 4400–4416, doi:10.1175/2007JAS2179.1.
- , 2012: A satellite study of the atmospheric forcing and response to moist convection over tropical and subtropical oceans. *J. Atmos. Sci.*, **69**, 150–167, doi:10.1175/JAS-D-11-016.1.
- , and T. S. L'Ecuyer, 2014: A mechanism of tropical convection inferred from observed variability in the moist static energy budget. *J. Atmos. Sci.*, **71**, 3747–3766, doi:10.1175/JAS-D-14-0015.1.
- , —, and C. D. Kummerow, 2006: The Madden-Julian oscillation recorded in early observations from the Tropical Rainfall Measuring Mission (TRMM). *J. Atmos. Sci.*, **63**, 2777–2794, doi:10.1175/JAS3783.1.
- Matsuno, T., 1966: Quasi-geostrophic motions in the equatorial area. *J. Meteor. Soc. Japan*, **44**, 25–43.
- Neelin, J. D., and I. M. Held, 1987: Modeling tropical convergence based on the moist static energy budget. *Mon. Wea. Rev.*, **115**, 3–12, doi:10.1175/1520-0493(1987)115<0003:MTCBOT>2.0.CO;2.
- , and J.-Y. Yu, 1994: Modes of tropical variability under convective adjustment and the Madden-Julian oscillation. Part I: Analytical theory. *J. Atmos. Sci.*, **51**, 1876–1894, doi:10.1175/1520-0469(1994)051<1876:MOTVUC>2.0.CO;2.
- Onogi, K., and Coauthors, 2007: The JRA-25 Reanalysis. *J. Meteor. Soc. Japan*, **85**, 369–432, doi:10.2151/jmsj.85.369.
- Peters, M. E., and C. S. Bretherton, 2006: Structure of tropical variability from a vertical mode perspective. *Theor. Comput. Fluid Dyn.*, **20**, 501–524, doi:10.1007/s00162-006-0034-x.
- Peters, O., and J. D. Neelin, 2006: Critical phenomena in atmospheric precipitation. *Nat. Phys.*, **2**, 393–396, doi:10.1038/nphys314.
- Raymond, D. J., 2000: Thermodynamic control of tropical rainfall. *Quart. J. Roy. Meteor. Soc.*, **126**, 889–898, doi:10.1002/qj.49712656406.
- , and Ž. Fuchs, 2007: Convectively coupled gravity and moisture modes in a simple atmospheric model. *Tellus*, **59A**, 627–640, doi:10.1111/j.1600-0870.2007.00268.x.
- , S. L. Sessions, A. H. Sobel, and Ž. Fuchs, 2009: The mechanics of gross moist stability. *J. Adv. Model. Earth Syst.*, **1** (9), doi:10.3894/JAMES.2009.1.9.
- Roundy, P. E., and W. M. Frank, 2004: A climatology of waves in the equatorial region. *J. Atmos. Sci.*, **61**, 2105–2132, doi:10.1175/1520-0469(2004)061<2105:ACOWIT>2.0.CO;2.
- Sessions, S. L., S. Sugaya, D. J. Raymond, and A. H. Sobel, 2010: Multiple equilibria in a cloud-resolving model using the weak temperature gradient approximation. *J. Geophys. Res.*, **115**, D12110, doi:10.1029/2009JD013376.
- Sherwood, S. C., 1999: Convective precursors and predictability in the tropical western Pacific. *Mon. Wea. Rev.*, **127**, 2977–2991, doi:10.1175/1520-0493(1999)127<2977:CPAPIT>2.0.CO;2.
- Simmons, A., S. Uppala, D. Dee, and S. Kobayashi, 2007: ERA-Interim: New ECMWF reanalysis products from 1989 onwards. *ECMWF Newsletter*, No. 110, ECMWF, Reading, United Kingdom, 25–35.
- Sobel, A. H., J. Nilsson, and L. M. Polvani, 2001: The weak temperature gradient approximation and balanced tropical moisture waves. *J. Atmos. Sci.*, **58**, 3650–3665, doi:10.1175/1520-0469(2001)058<3650:TWTGAA>2.0.CO;2.
- , S. Wang, and D. Kim, 2014: Moist static energy budget of the MJO during DYNAMO. *J. Climate*, **71**, 4276–4291, doi:10.1175/JAS-D-14-0052.1.
- Takayabu, Y., 1994a: Large-scale cloud disturbances associated with equatorial waves. I: Spectral features of the cloud disturbances. *J. Meteor. Soc. Japan*, **72**, 433–449.
- , 1994b: Large-scale cloud disturbances associated with equatorial waves. Part II: Westward-propagating inertio-gravity waves. *J. Meteor. Soc. Japan*, **72**, 451–465.
- , K.-M. Lau, and C.-H. Sui, 1996: Observation of a quasi-2-day wave during TOGA COARE. *Mon. Wea. Rev.*, **124**, 1892–1913, doi:10.1175/1520-0493(1996)124<1892:OOAQDW>2.0.CO;2.
- Tulich, S. N., and G. N. Kiladis, 2012: Squall lines and convectively coupled gravity waves in the tropics: Why do most cloud systems propagate westward? *J. Atmos. Sci.*, **69**, 2995–3012, doi:10.1175/JAS-D-11-0297.1.
- Wheeler, M., and G. N. Kiladis, 1999: Convectively coupled equatorial waves: Analysis of clouds and temperature in the wavenumber–frequency domain. *J. Atmos. Sci.*, **56**, 374–399, doi:10.1175/1520-0469(1999)056<0374:CCEWAO>2.0.CO;2.
- , —, and P. J. Webster, 2000: Large-scale dynamical fields associated with convectively coupled equatorial waves. *J. Atmos. Sci.*, **57**, 613–640, doi:10.1175/1520-0469(2000)057<0613:LSDFAW>2.0.CO;2.
- Yanai, M., S. Esbensen, and J.-H. Chu, 1973: Determination of bulk properties of tropical cloud clusters from large-scale heat and moisture budgets. *J. Atmos. Sci.*, **30**, 611–627, doi:10.1175/1520-0469(1973)030<0611:DOBPOT>2.0.CO;2.
- , B. Chen, and W.-W. Tung, 2000: The Madden-Julian oscillation observed during the TOGA COARE IOP: Global view. *J. Atmos. Sci.*, **57**, 2374–2396, doi:10.1175/1520-0469(2000)057<2374:TMJOOD>2.0.CO;2.
- Yasunaga, K., and B. Mapes, 2012a: Differences between more divergent and more rotational types of convectively coupled equatorial waves. Part I: Space–time spectral analyses. *J. Atmos. Sci.*, **69**, 3–16, doi:10.1175/JAS-D-11-033.1.
- , and —, 2012b: Differences between more divergent and more rotational types of convectively coupled equatorial waves. Part II: Composite analysis based on space–time filtering. *J. Atmos. Sci.*, **69**, 17–34, doi:10.1175/JAS-D-11-034.1.
- , and —, 2014: Differences between faster versus slower components of convectively coupled equatorial waves. *J. Atmos. Sci.*, **71**, 98–111, doi:10.1175/JAS-D-13-03.1.